Agenzia nazionale per le nuove tecnologie,
l'energia e lo sviluppo economico sostenibile

MINISTERO DELLO SVILUPPO ECONOMICO

Ricerca di Sistema elettrico

Simulazione Numerica Diretta Del Bruciatore ROMULUS per lo Studio della Combustione CH4/Aria in Ambiente Ricco di CO2

D. Cecere, E. Giacomazzi, N. Arcidiacono, F.R. Picchia

Report RdS/PAR2017/192

SIMULAZIONE NUMERICA DIRETTA DEL BRUCIATORE ROMULUS PER LO STUDIO DELLA COMBUSTIONE CH_4/ARIA IN AMBIENTE RICCO DI CO_2

D. Cecere, E. Giacomazzi, N. Arcidiacono, F.R. Picchia (ENEA, DTE-PCU-IPSE)

Settembre 2018

Report Ricerca di Sistema Elettrico
Accordo di Programma Ministero dello Sviluppo Economico - ENEA
Piano Annuale di Realizzazione 2017
Area: Generazione di energia con basse emissioni di carbonio
Progetto B.2: Polo Tecnologico del SULCIS: Tecnologie e Metodologie "Low Carbon" e Edifici ad Energia Quasi Zero (nZEB)
Obiettivo: Parte A1 - a.1 - Cicli TurboGas EGR
Task a.1.3 – Studi mediante Simulazione Numerica (HeaRT)
di processi di ossi-combustione in condizioni EGR
Responsabile del Progetto: Franca Rita Picchia, ENEA

Indice

Sommario **4**

1 The Code HeaRT and governing Equations **7**
1.0.1 Physical Properties and Kinetic Model 8

2 Experiment configuration **9**
2.1 Results 10
2.1.1 Displacement speeds 13

3 Conclusions **17**

Referenze **20**

Sommario

Nell'ambito dello studio di cicli turbo-gas non convenzionali EGR, (task 3 della presente annualità) si è provveduto ad effettuare, tramite il codice proprietario HEART, la simulazione diretta dell'apparato sperimentale Romulus, il successivo confronto con i dati sperimentali a disposizione e l'ottenimento di ulteriori grandezze caratteristiche della fiamma non facilmente ottenibili da risultati sperimentali. Nella configurazione attuale il flusso di combustibile premiscelato è rappresentato da CH_4 , è stato simulato con tecnica DNS attraverso l'utilizzo del codice proprietario HEART. Il getto di combustibile fluisce ad una velocità di circa 17 m/s attraverso un canale rettangolare posto al centro della parte inferiore della camera di combustione. La camera di combustione ha forma di un parallelepipedo (0.01 mx0.027 mx0.1 m). Il canale di immissione del combustibile (0.003 mx0.01 m a sezione rettangolare) è circondato da due piastre forate. Attraverso queste ultime vengono iniettati i gas caldi costituiti dai prodotti di combustione di una fiamma laminare stechiometrica di propano, le cui caratteristiche sono rappresentate in Fig 0.1.

Lo schema cinetico utilizzato nella seguente simulazione presenta 17 specie chimiche differenti e 73 reazioni elementari. Le condizioni al contorno di velocità nulla e di gradiente nullo di pressione sono stati imposti sulle pareti della camera di combustione, mentre all'uscita del combustore (all'altezza di z = 0.075m) sono state imposte condizioni al contorno non riflessive. All'ingresso del condotto di immissione del combustibile le fluttuazioni di velocità sono state imposte attraverso la procedura di Klein per la produzione di turbolenza sintetica. In Fig. 0.2 è mostrata una iso-superficie istantanea di temperatura ad un valore di circa 1800K. Questa superficie rappresenta in prima approssimazione la superficie dove sostanzialmente avviene la reazione chimica ed individua, quindi, la posizione del cosiddetto fronte di fiamma. La fiamma pertanto presenta una forma conica della lunghezza massima di circa 0.055 m, in accordo con quanto si è misurato sperimentalmente. La lunghezza della fiamma, comunque, non è costante lungo la direzione x (essendo più corta vicino alle pareti e dell'ordine dei 0.02 m), questo prova l'effetto delle pareti sulla fiamma stessa e quindi la necessità di una griglia adeguata lungo questa direzione in prossimità delle pareti per descrivere correttamente il profilo di velocità. Alle condizioni di ingresso della velocità assegnate, il numero di Reynolds, basato sul raggio idraulico della sezione di ingresso del combustibile, risulta essere pari a 5000. A queste condizioni il flusso risulta essere turbolento, come è possibile osservare dalla iso-superficie in Fig. 0.2 che, a causa delle strutture vorticose iniettate all'ingresso e sviluppatesi all'interno del canale, corrugano la fiamma attraverso interazioni turbolenza/fronte di fiamma. In Figura 3 sono mostrate invece immagine del campo medio di temperatura in un piano di normale x ad x=0 assieme alle linee di flusso del campo di velocità. Poiché la sezione di passaggio del flusso diminuisce a causa dello strato limite che si forma all' interno del condotto di immissione del combustibile, la velocità aumenta rispetto a quella nominale di ingresso e raggiunge picchi di circa 23 m/s. Inoltre a causa della presenza delle pareti, all'uscita del condotto del combustibile si formano delle bolle di ricircolo, come si può osservare dalla figura 3b (che riportata una immagine media del rilascio di calore in W/m3) , dove sono presenti velocità negative dell'ordine di 0.39 m/s. In Fig. 0.3 a invece è rappresentata la temperatura media nel piano di normale x ad x=0. Come si vede la camera di combustione è per lo più riempita di gas caldi ad una temperatura di circa 2250 K, grazie anche all'azione dei grandi vortici di ricircolo che si formano lateralmente (della dimensione si circa 0.01 m), e solo la parte di volume contenuta all'interno del cono a base rettangolare ed altezza pari a circa 0.05 m presenta temperature inferiori (vedi Fig.3a) fino ad un minimo di 300 K (che è la temperatura a cui viene iniettata la miscela in camera di combustione). Profili medi di velocità sono stati confrontati con quelli sperimentali, mentre la struttura della fiamma è stata analizzata attraverso statistiche sulla curvatura e Flame Displacement Speed.

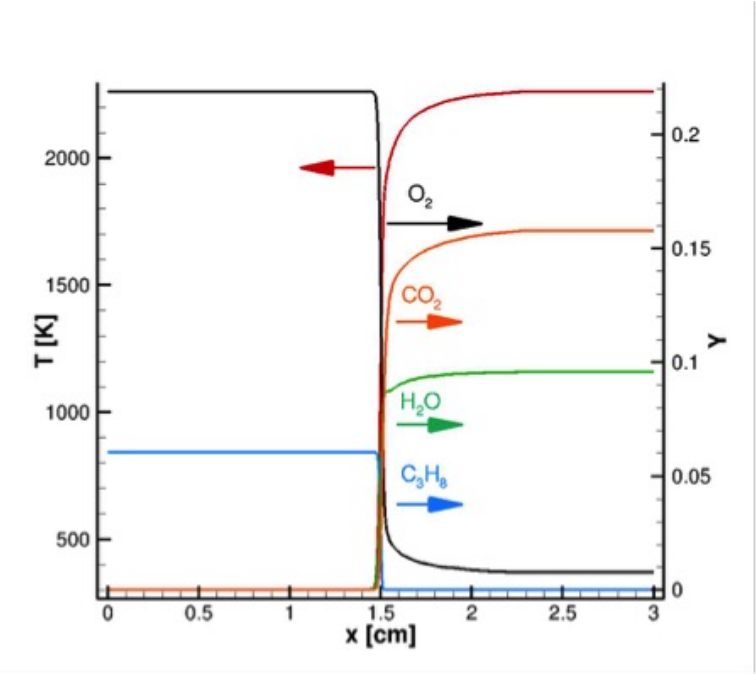

Figura 0.1: Soluzione della fiamma laminare stechiometrica Propano/aria: profilo di Temperatura e delle maggiori specie chimiche.

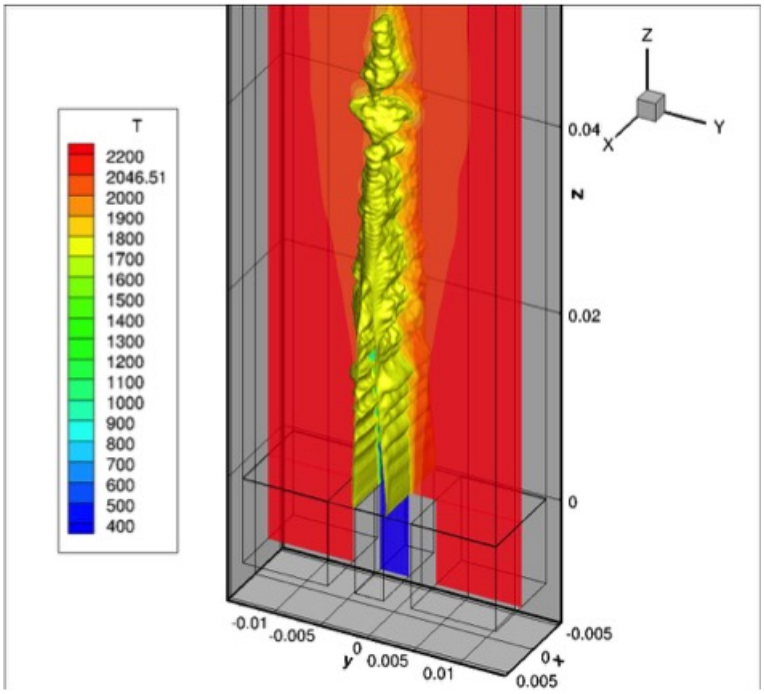

Figura 0.2: Isosuperficie istantanea della temperatura (1800 K) . Slice di un piano di normale x a x=0, e dominio di calcolo.

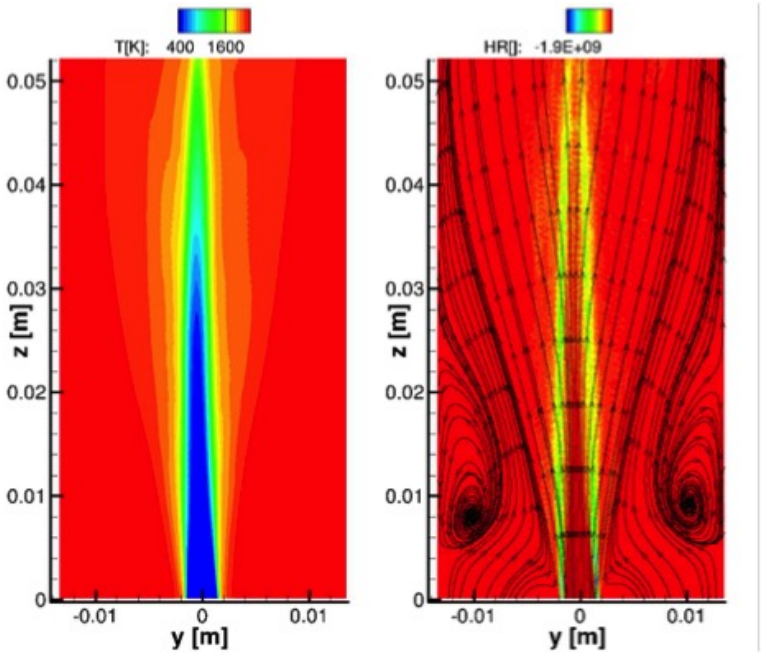

Figura 0.3: Slices di un piano di normale x a x=0, a) Temperatura media con linee di flusso; b) Campo medio del rilascio di calore [W/m3].

1 The Code HeaRT and governing Equations

Gaseous combustion is governed by a set of transport equations expressing the conservation of mass, momentum and energy, and by a thermodynamic equation of state describing the gas behaviour. The numerical simulations are performed by means of the in-house parallel code HeaRT and ENEA's supercomputing facility CRESCO [1]. The HeaRT code solves the compressible Navier-Stokes equations discretised through staggered finite-difference schemes. A second-order accurate centered scheme is adopted for diffusive fluxes; convective terms are modelled through the $AUSM^{+}$-up method [2] coupled with a third/fifth-order accurate $WENO$ interpolation to reduce spurious oscillations; such numerical spatial scheme was extensively tested by the present authors proving its robustness and accuracy [3]. The low-storage third-order accurate Runge-Kutta method of Shu-Osher is used for time integration. The total energy is defined as sum of internal (thermal) and kinetic energy only. The authors found this choice mandatory [4, 5] to avoid, or at least reduce, unphysical energy and temperature oscillations, mainly driving to the divergence of calculation. No spurious waves were experienced in previous simulations of premixed flames, when the total energy was defined including the chemical formation contribution. For a mixture of N_s ideal gases in local thermodynamic equilibrium but chemical nonequilibrium, the corresponding filtered field equations (extended Navier−Stokes equations) are:

- Transport Equation of Mass

$$\frac{\partial \rho}{\partial t} + \frac{\partial \rho u_i}{\partial x_i} = 0. \tag{1.1}$$

- Transport Equation of Momentum

$$\frac{\partial (\rho u_j)}{\partial t} + \frac{\partial (\rho u_i u_j + p\delta_{ij})}{\partial x_i} = \frac{\partial \tau_{ij}}{\partial x_i} \tag{1.2}$$

- Transport Equation of Total Energy (internal + mechanical, $\mathcal{E} + \mathcal{K}$)

$$\frac{\partial (\rho \mathcal{U})}{\partial t} + \frac{\partial (\rho u_i \mathcal{U} + p u_i)}{\partial x_i} = -\frac{\partial (q_i - u_j \tau_{ij})}{\partial x_i} \tag{1.3}$$

- Transport Equation of the N_s Species Mass Fractions

$$\frac{\partial (\rho Y_n)}{\partial t} + \frac{\partial (\rho u_j Y_n)}{\partial x_i} = -\frac{\partial}{\partial x_i}(J_{n,i}) + \dot{\omega}_n \tag{1.4}$$

- Thermodynamic Equation of State

$$p = \rho \sum_{n=1}^{N_s} \frac{Y_n}{W_n} \mathcal{R}_u T \tag{1.5}$$

These equations must be coupled with the constitutive equations which describe the molecular transport. In the above equations, t is the time variable, ρ the density, u_j the velocities, τ_{ij} the viscous stress tensor, $\mathcal{U}$ the total filtered energy per unit of mass, that is the sum of the filtered internal energy, $\widetilde{e}$, and the resolved kinetic energy, $1/2\, u_i u_i$, q_i is the heat flux, p the pressure, T the temperature, $\mathcal{R}_u$ is the universal gas constant, W_n the nth-species molecular weight, $\dot{\omega}_n$ is the production/destruction rate of species n, diffusing at velocity $V_{i,n}$ and resulting in a diffusive mass flux $\boldsymbol{J_n} = \rho Y_n \boldsymbol{V_n}$. The stress tensor and the heat flux are respectively:

$$\tau_{ij} = 2\mu \left(S_{ij} - \frac{1}{3} S_{kk} \delta_{ij}\right) \tag{1.6}$$

$$q_i = -k \frac{\partial T}{\partial x_i} + \rho \sum_{n=1}^{N_s} h_n Y_n V_{i,n}. \tag{1.7}$$

In Eqn. 1.6-1.7 μ is the molecular viscosity and k is the termal conductivity.

Non-reflecting boundary conditions [6, 7, 8] are implemented at open boundaries in their extended form to take into account the effect of variable transport properties [9], local heat release [10] and real gas effects [11]. It is observed that in previous and present real gas simulations the authors had to impose a higher value of the relaxation constant in the partially non-reflecting treatment of the outlet with respect to the ideal gas theoretical value (1.5 against 0.27) [6, 12] to avoid unphysical pressure drift in the whole computational domain. A synthetic turbulence generator is adopted at flow inlets [13].

1.0.1 Physical Properties and Kinetic Model

Kinetic theory is used to calculate dynamic viscosity and thermal conductivity of individual species [14]. The mixture-average properties are estimated by means of Wilke's formula with Bird's correction for viscosity [15, 16], and Mathur's expression for thermal conductivity [17].

Eqn. 1.7, the first term is the heat transfer by conduction, modeled by Fourier's law, the second is the heat transport due to molecular diffusion acting in multicomponent mixtures and driven by concentration gradients. The Hirschfelder and Curtiss approximate formula for mass diffusion $\boldsymbol{V_n}$ in a multicomponent mixture is adopted, i.e.,

$$\begin{aligned} \boldsymbol{J_n} = \rho Y_n \boldsymbol{V_n} &= -\rho Y_n \sum_{i=1}^{N_s} D^{\star}_{nj} \boldsymbol{d_n} - D^T_n \frac{\nabla T}{T} \\ &= -\rho \frac{W_n}{W_{mix}} D_n \nabla X_n - D^T_n \frac{\nabla T}{T} \ , \end{aligned} \tag{1.8}$$

with $X_n = Y_n W_{mix}/W_n$ and the D_n is

$$D_n = \frac{1 - Y_n}{\sum_{j=1,\, j\neq n}^{N_s} \frac{X_j}{\mathcal{D}_{jn}}} \ . \tag{1.9}$$

$\mathcal{D}_{jn}$ being the binary diffusion coefficient and D^T_n is the n-th species thermo diffusion coefficient and $\boldsymbol{d_n}$ the diffusional driving forces that for low-density gases became:

$$\boldsymbol{d_n} = \nabla X_n + (X_n - Y_n) \frac{\nabla p}{p} \frac{\rho}{p} \sum_{i=1, i\neq n}^{N_s} Y_i Y_n (\boldsymbol{f_i} - \boldsymbol{f_n}) \tag{1.10}$$

Only the first cross diffusion term of Eqn. 1.10 is retained in this work, while the pressure gradient diffusion (low subsonic flame flow) and the external forces diffusion (low-density gases assumption) are neglected.

When inexact expressions for diffusion velocities are used (as when using Hirschfelder's law), and in general when differential diffusion effects are considered, the constrain $\sum_{i=1}^{N_s} \boldsymbol{J_i} = \sum_{i=1}^{N_s} \rho Y_i \boldsymbol{V_i} = 0$ is not necessarily satisfied. In this paper, to impose mass conservation, an artificial diffusion velocity $\boldsymbol{V^c}$ is subtracted from the flow velocity in the species transport equations [18]. This velocity, assuming Hirschfelder's law holds, becomes:

$$\boldsymbol{V^c} = -\sum_{n=1}^{N_s} \frac{W_n}{W_{mix}} D_n \nabla X_n \ . \tag{1.11}$$

in the progress variable space. For the flame considered the only elements present are carbon, hydrogen, oxygen and nitrogen: m = C, H, O, N and the local equivalence ratio ϕ is calculated as:

$$\phi = \frac{2A_C + 0.5A_H}{A_O} \tag{1.12}$$

where $A_m = \sum_{k=1}^{K} \alpha_{k,m} x_k$ is the number of moles of atom of element m per mole of gas, $\alpha_{k,m}$ the number of atoms of element m per species k and x_k its mole fraction.

2 Experiment configuration

The simulation was performed in a slot-burner Bunsen flame configuration. The slot-burner Bunsen configuration is especially interesting due to the presence of mean shear in the flow and is similar in configuration to the burner used in experimental studies.

This configuration consists of a central reactant jet through which premixed reactants are supplied. The central jet is surrounded on either side by a heated coflow, whose composition and temperature are those of the complete combustion products of a stoichiometric C_3H_8/Air freely propagating mixture. The reactant jet was chosen to be a premixed methane/ air jet at 300 K and mixture equivalence ratio $\phi = 1.0$, the adiabatic flame temperature of the products gas is 2254 K. The unstrained laminar flame properties at these conditions

ϕ	T_u [K]	T_b [K]	s_L[cm s^{-1}]	δ_{th}[mm]
1.0	300	2254	35.75	0.320

Tabella 2.1: CH_4/H_2 − Air laminar flame.

computed using Chemkin are summarized in Table 2.1. In this table ϕ represents the multicomponent equivalence ratio of the reactant jet mixture, T_u is the unburned gas temperature, T_b the products gas temperature, s_L represents the unstrained laminar flame speed and $\delta_{th} = (T_b - T_u)/|\partial T/\partial x|_{max}$ is the thermal thickness based on maximum temperature gradient. Preheating the reactants leads to a higher flame speed and allows a higher inflow velocity without blowing out the flame, reducing computational costs. Also, many practical devices such as gas turbines, internal combustion engines, and recirculating furnaces operate at highly preheated conditions (EGR conditions). The simulation parameters are summarized in Table 2.2.

Slot width (h)	3.0 mm
Domain size in the spanwise (L_x), crosswise (L_y) and streamwise (L_z) directions	$3.3h \times 10h \times 23h$
$N_x \times N_y \times N_z$	$1968 \times 400 \times 240$
Turbulent jet velocity (U_0)	17 $m\ s^{-1}$
Coflow velocity	0.54 m s^{-1}
Jet Reynolds Number ($Re_{jet} = U_0 h/\upsilon$)	5000
Turbulent intensity (u'/S_L)	4.59
Turbulent length scale (l_t/δ_L)	2.6
Minimum grid space	20μm
Kolmogorov Lenght Scale η_K	27.22 μm

Tabella 2.2: CH_4 − Air turbulent flame: the kinematic viscosity used in the calculation of Reynolds number is that of the inflow CH_4/Air mixture $\nu = 1.3 \cdot 10^{-5}$ m^2 s^{-1}

The domain size in the streamwise (z), crosswise (y) and spanwise (x) directions is $L_x \times L_y \times L_z = 3.3h \times 10h \times 23h$, h being the slot width (h = 3mm). The grid is uniform only in the x direction ($\Delta x = 20\mu$m), while is stretched in the y and z direction near the inlet duct walls. The DNS was run at atmospheric pressure using a 17 species and 73 elementary reactions kinetic mechanism [19]. The mean velocity of the central jet stream is 17 m/s, while the velocity of the coflow stream is 0.54 m/s. The width h of the central duct, where the inlet turbulent velocity profile may develop, is 3 mm and 10 mm long. The width walls of the duct h_w is 3 mm. Velocity streamwise fluctuations, $u'_z = 1.7$ ms^{-1}, are imposed on the mean inlet duct's velocity profile by means of Klein's procedure [13]. The jet Reynolds number based on the centerline inlet velocity and slot width h is $Re_{jet} = Uh/\upsilon = 5000$. Based on the jet exit duct centerline velocity and the total streamwise domain lenght, the flow through time is $\tau_U = 3.2\,ms$. Navier-Stokes characteristic boundary conditions (NSCBC) were adopted to

prescribe boundary conditions. Periodic boundary conditions were applied in the x direction, while improved staggered non-reflecting inflow and outflow boundary conditions were fixed in y and z directions [8]. The simulation was performed on the linux cluster CRESCO 6 (Computational Center for Complex Systems) at ENEA, requiring 1.5 million CPU-hours running for 60 days on 3500 processors. The solution was advanced at a constant time step of 4.9 ns and after the flame reached statistical stationarity, the data were been collected through 4 τ_U.

2.1 Results

An overall description of the slot flame is given by the evolution, downstream the inlet channel, of the axial and radial velocities $\widetilde{U}_z, \widetilde{U}_y$ shown in Fig. 2.1. The symbol $\widetilde{\phi}$ indicates Favre mean of the variable ϕ defined as $\widetilde{\phi}(y,z) = \overline{\rho\phi}/\overline{\rho}$, where ρ is the density and the overbar denotes ensemble averages defined as:

$$\overline{\phi}(y,z) = \frac{1}{N_d N_x} \sum_{n=1}^{N_d} \sum_{k=1}^{N_x} \phi(x_k, y, z, t_n). \tag{2.1}$$

with N_d is the number of data sets in a statistically stationary time period (approximately $\sim 8T_c = L_z/U_0$), N_d is the number of grid points in the x periodic direction. At the exit of the channel, the axial velocity U_z reach a maximum value of 121ms^{-1} greater than its inlet value ($17m/s$), due to formation of the channel boundary layer, that is equivalent to a restriction of the flow section (see Fig.2.1b). At the exit of the central nozzle, the jet, surrounded by the hot coflow, expands and at higher heights the streamlines diverge towards greater y. Due to the presence of wall, a great recirculation region is formed at an height of approximately 0.01m with a diameter of 0.005 m. The radial velocity of this vortex is approximately of 0.36ms^{-1}. This vortex is responsible,

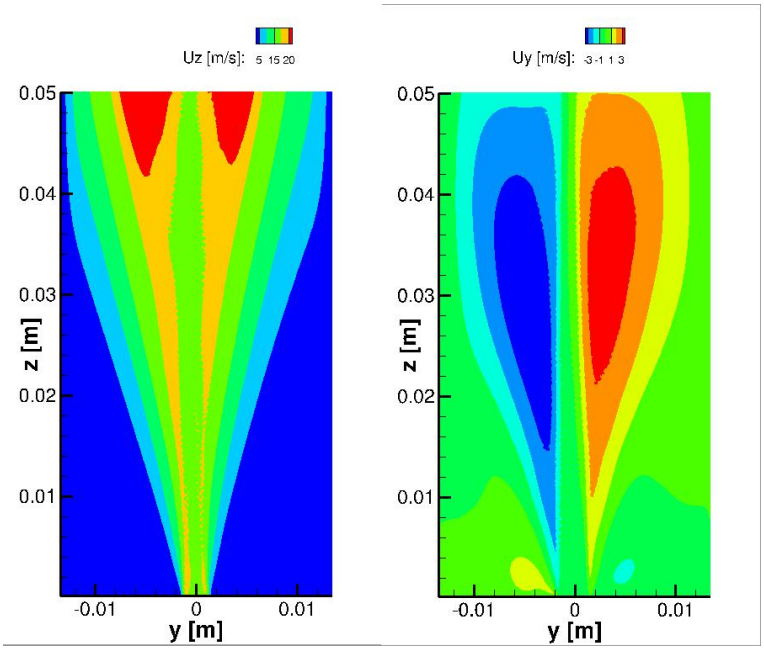

Figura 2.1: Mean streamwise and radial velocity profiles [m/s] at x=0 plane.

together with local turbulence, of the mixing of the C_3H_8 hot products with fresh mixture. This region is not evidenced by experimental measurements. In this region, since the PIV-Alumina particles are seeded inside the fresh CH_4 mixture, in this region their concentration is very small and the signal to noise ratio is very small to obtain experimental velocity. This is one of the first advantages of a Direct Numerical Simulation, showing phenomena that experiments can't do. As shown in Fig. 2.2a the flame has a height of approximately 5 cm (based on the position of the maximum heat release isosurface on the progress variable isosurface c=0.7) and a mean conical shape. It is surrounded by the Propane hot products and this promotes reaction and stabilizes

the flame, increasing enthalpy by heat exchange. Fig.2.3 shows the mean species profile (H_2O, HCO, OH)

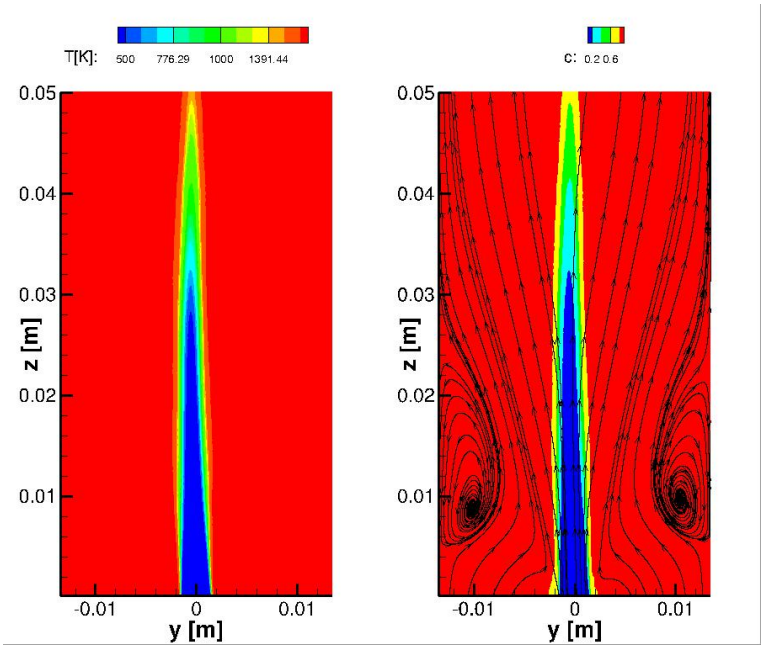

Figura 2.2: Mean temeperature [K] and progress variable with streamlines at x=0 plane.

and so the position of the mean flame front (HCO, OH), the flame is continuous from the mixture jet exit to its tip (0.05m), H_2O fills all the combustion chamber. Anyway the length of the flame depends from the x

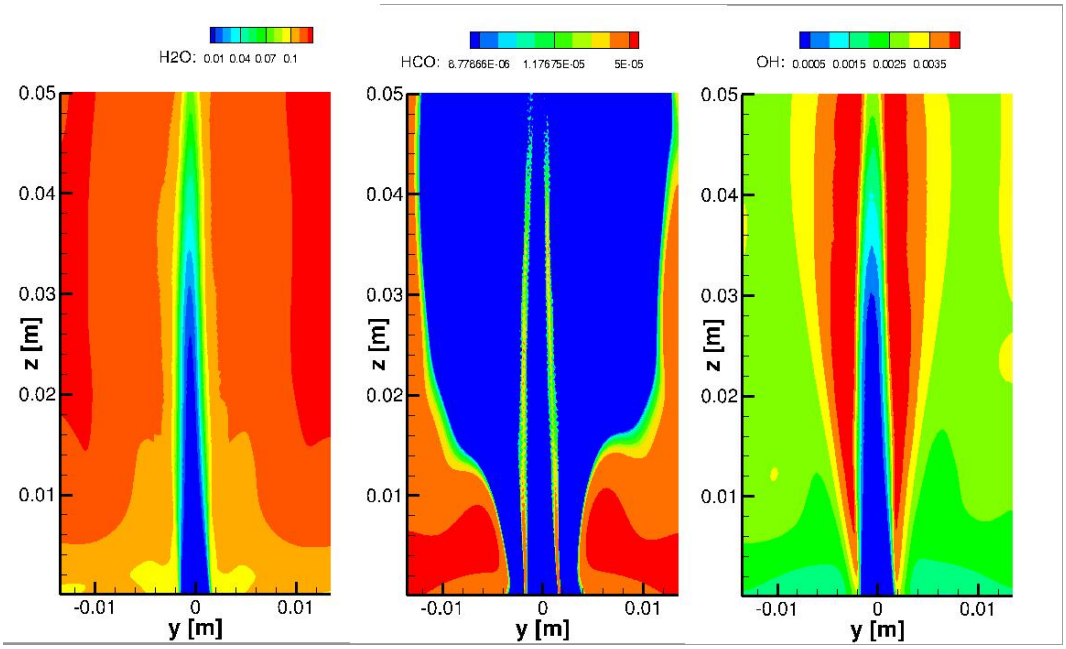

Figura 2.3: Mean species profile at x=0 plane.

position as shown in Fig.2.4, i.e. it depends from the distance from the wall ($x = -0.005$ m and $x = 0.005$ m). At $x = -0.005$morx $= 0.005$m the flame starts at $z = 0.026$ m and reach its aximum length at $x = 0$ m.

Fig.2.5 shows streamwise velocity profiles at different heights and their comparison with PIV experimental results. The DNS data shows an under prediction of the peak temperature, althoughthey show the typical turbulent flat profile. This may be due to the approximation of the flux experimental data and to the not

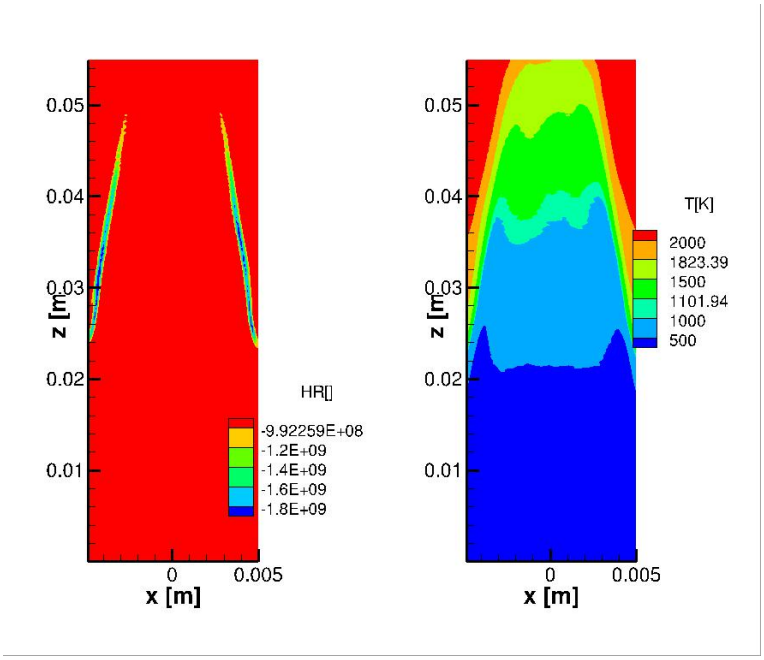

Figura 2.4: Mean heat release rate and temperature profile at y=0 plane.

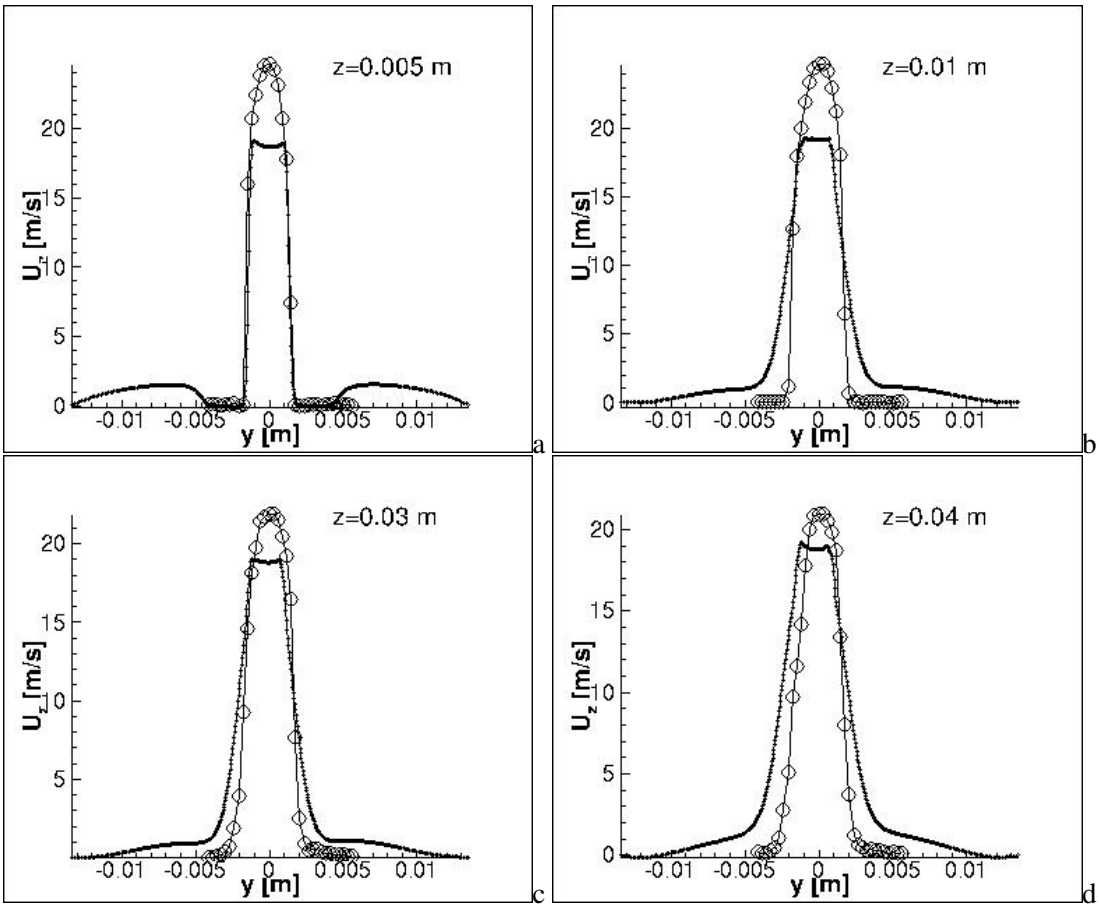

Figura 2.5: Mean streamwise velocity profile at x=0 plane and at different heigths.

completely developed DNS inlet channel (the boundary layer it is not completely developed and DNS fails the effective restriction of inlet channel due to boundary conditions). Anyway experimental results are not able to give the complete velocity profile, (for $|y| > 0.006\,\mathrm{m}$) since for this position the laser signal to noise ratio is very low and no data are available in these regions.

2.1.1 Displacement speeds

Under the assumptions that a turbulent premixed flame retains locally the structure of a laminar flame but stretched and wrinkled by the surrounding turbulence, it is possible to separate the non linear nature of turbulence with that of the reaction rate defining a reaction progress variable, monotonically varying from 0 in the fresh reactants to 1. The flame zones are identified with progress variable isosurfaces, on which statistics are extracted. Once the species that define the normalized progress variable c are determined (in this case $H_2O + CO_2$), if Differential Diffusion is taken into account and Hirschfelder and Curtiss formula for mass diffusion and Soret effect are included (Eqn.1.8), the normalized progress variable transport equation must be revised as:

$$\begin{aligned}\frac{\partial c}{\partial t} + \boldsymbol{u}\cdot\nabla c = &\frac{1}{\rho Y_{c,n}}\Big(\sum_{i\in S}\nabla\cdot\Big(\rho\frac{W_i}{W_m}D_i\nabla X_i\Big)+\\ &\sum_{i\in S}\nabla\cdot\Big(\frac{D_i^T}{T}\nabla T\Big)+\dot{\omega}_c\Big)\end{aligned} \tag{2.2}$$

with W_m the average mixture molecular weight, $\dot{\omega}_c = \sum_{i\in S}\dot{\omega}_i$ and $Y_{c,n}$ defined in Eqn. **??**. The mass diffusion term of Eqn. 2.2 based on the Hirschfelder and Curtiss formula may be split into a normal and tangential term recognizing that

$$\nabla X_i = \frac{W_m}{W_i}\nabla Y_i + \frac{Y_i}{W_i}\nabla W_m \tag{2.3}$$

with $\nabla Y_i = -|\nabla Y_i|\boldsymbol{n}$. Further expansion of the divergence operator, $\nabla\cdot()$, yields for Eqn.2.2 to:

$$\begin{aligned}&\frac{\partial c}{\partial t} + \boldsymbol{u}\cdot\nabla c =\\ &\frac{1}{\rho Y_{c,n}}\sum_{i\in S}\Big(-\boldsymbol{n}\cdot\nabla(\rho D_i|\nabla Y_i|) - \rho D_i|\nabla Y_i|\nabla\cdot\boldsymbol{n} + \nabla\cdot\Big(\frac{\rho D_i Y_i}{W_m}\nabla W_m\Big)\Big)+\\ &\frac{1}{\rho Y_{c,n}}\sum_{i\in S}\nabla\cdot\Big(\frac{D_i^T}{T}\nabla T\Big) + \frac{\dot{\omega}_c}{\rho Y_{c,n}}\end{aligned} \tag{2.4}$$

Here, $\nabla\cdot\boldsymbol{n}$ is the curvature which may be expressed as the sum of the local inverses of the principal radii of curvature of the isosurface and flame surface curved convex towards the reactants is assumed to have positive curvature. The same equation can be written in kinematic form for a progress variable isosurface $c = c^*$ [20]:

$$\Big[\frac{\partial c}{\partial t} + \boldsymbol{u}\cdot\nabla c\Big]_{c=c^*} = S_d|\nabla|_{c=c^*} \tag{2.5}$$

where S_d, the displacement speed, is the magnitude of the propagation velocity of the isocontour with normal $\boldsymbol{n} = -(\nabla c/|\nabla c|)_{c=c^*}$ directed toward the unburnt gas. Considering Eqns. (2.2-2.5) the following expression for the displacement speed S_d is obtained:

$$
\begin{aligned}
S_d = [\frac{1}{\rho|\nabla c|Y_{c,n}}(\omega_c + \\
&\sum_{i\in S}(-\boldsymbol{n}\cdot\nabla(\rho D_i|\nabla Y_i|)) + \\
&\sum_{i\in S}(-\rho D_i|\nabla Y_i|\nabla\cdot\boldsymbol{n}) + \\
&\sum_{i\in S}(\nabla\cdot(\frac{\rho D_i Y_i}{W_m}\nabla W_m)) + \\
&\sum_{i\in S}\nabla\cdot(\frac{D_i^T}{T}\nabla T))]_{c=c^*}.
\end{aligned}
\tag{2.6}
$$

This expression shows that $S_d = S_r + S_n + S_t + S_h + S_{td}$ is determined by the sum of five contributions: (a) reaction of progress variable, (b) normal mass diffusion, c) tangential mass diffusion, d) a new term related to Hirschfelder and Curtiss formula for mass diffusion, e) thermal diffusion.

The last two term are not splitted in the iso-c normal and tangential components since the iso-c normal and iso-T normal are generally not parallel. The value of the displacement speed changes across the flame normal because of thermal expansion effects, using a density-weighted displacement speed $S_d^* = \rho S_d/\rho_u$ this effect may be largely reduced.

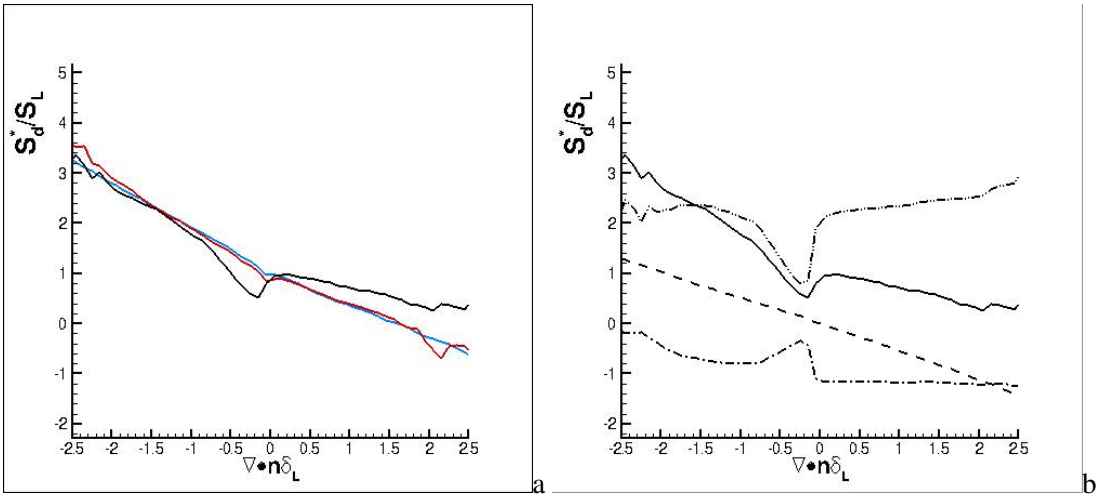

Figura 2.6: a) Mean (averaged on intervals of curvature) density weighted displacement speed S_d^*/S_L plotted against the normalized curvature $\nabla\cdot\boldsymbol{n}\delta_L$ at (blue line) c=0.4, (red line) c =0.6, (black) c=0.76; b) Mean displacement speed and its components at a representative value of reaction progress variable c=0.76, (dash dot dot line) S_r, (dashed line) S_t, (dashed dot line) S_n.

Fig. 2.6a-b shows the mean (averaged on intervals of curvature) density weighted displacement speed S_d^*/S_L plotted against the normalized curvature $\nabla\cdot\boldsymbol{n}\delta_L$ at a representative values of reaction progress variable (blue line) c=0.4, (red line) c =0.6, (black) c=0.76.

The data shown in Fig.2.6a reveal a scatter at high values of curvature $\nabla\cdot\boldsymbol{n}\delta_L > 2.5$): this is associated with the relatively low number of points in this range of curvature within the flame brush (see PDF of curvature in Fig.2.7) and therefore are excluded from the representation.

Curvature and flame displacement speed are negatively correlated with a strong variation across the flame brush and, flame elements with negative curvatures (curvature center in the unburnt mixture) propagate with faster flame speed than positively curved elements as shown in Fig.2.6a-b. Generally, the negative correlation of the total displacement speed S_d^*/S_L is stronger at negative curvatures and this asymmetry may be explained by the same asymmetric trend of the $|\nabla c|$ versus curvature and at the relation of S_d^*/S_L with $|\nabla c|$ in Eq.2.6.

The local geometry of the progress variable scalar field is defined by its value c(x, t), its derivative in the direction normal to the iso-surface and its curvature.

Flame curvatures are computed from the asymmetric tensor formed by taking the gradient of the flame front normal vector: $n_{i,j} = \partial n_i / \partial x_j$. The principal curvatures k_1, k_2 are the two nonzero eigenvalues of the curvature tensor $n_{i,j}$. They are related to the two nonzero invariants $I_1 = -\nabla \cdot \mathbf{n} = -(k_1 + k_2) = 2k_m$ ($k_m = I_1/2$ being the mean curvature) and $I_2 = (n_{i,i}n_{j,j} - n_{i,j}n_{j,i})/2 = k_1 k_2 = k_g$ (the Gaussian curvature) by $k_1, k_2 = \left(-I_1 \pm \sqrt{I_1^2 - 4I_2}\right)/2$. Regions having $k_g > k_m^2$ implies complex curvature and they are excluded from the statistics.

Statistics of the curvature, normalized using the respective laminar flame temperature gradient thickness δ_L and accumulated on different iso-c surfaces are shown in Fig. 2.7a.

Averaging over intervals of curvature has been performed to reduce data scattering, and the trend is not sensitive to the adopted interval. Looking at Fig. 2.7a, it is observed that in the reaction layer but, at lower c, (see the $c = 0.7$ curves) of the flame, it is high the probability of finding negative curvatures. This probability decreases at greater values of c and a significant PDF asymmetry, towards positive curvatures, is observed.

In order to investigate the effect of differential and thermal diffusion associated with light species as H_2 and H on local mixture equivalence ratio, this quantity is calculated via Eq. (1.12) and shown in Fig. 2.7b as a function of the normalized curvature at different values of the progress variable.

The equivalence ratio Φ is positively correlated with curvature at all progress variable iso-surfaces; the strongest variation is seen in the reaction zone ($c \sim 0.76$). This positive correlation can be explained by considering that H_2 and H are preferentially focused into areas with positive curvature and defocused from areas of negative curvature.

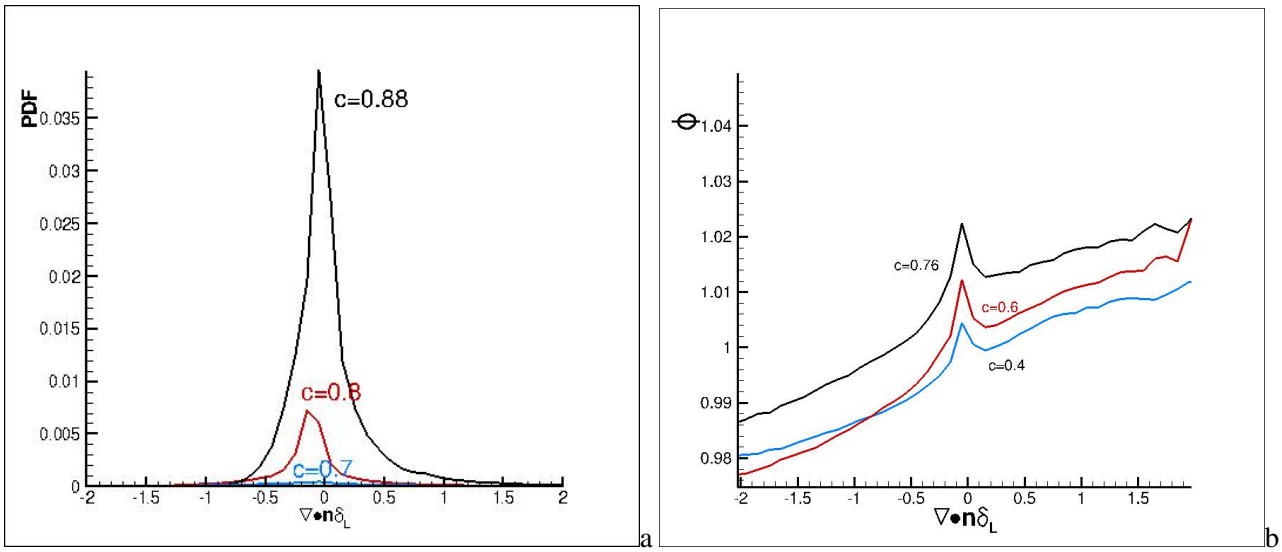

Figura 2.7: a) Probability Density Function (PDF) of the normalized curvature at different progress variable values (blue line) c = 0.4, (red line) c = 0.6, (black) c = 0.76 of the flame; b) Equivalence ratio at different levels of the progress variable c as a function of the normalized curvature: (blue line) c=0.4, (red line) c =0.6, (black) c=0.76;

Fig. 2.8 shows an isosurface of temperature at 1850 K and a slice of OH mass fraction. It is observed that, due to curvature effects and so to heat concentration, the maximum values of OH mass fraction are located at positive curvature where the mixture gases are preheated by surrounding flame and source rates are improved by increased enthalpy.

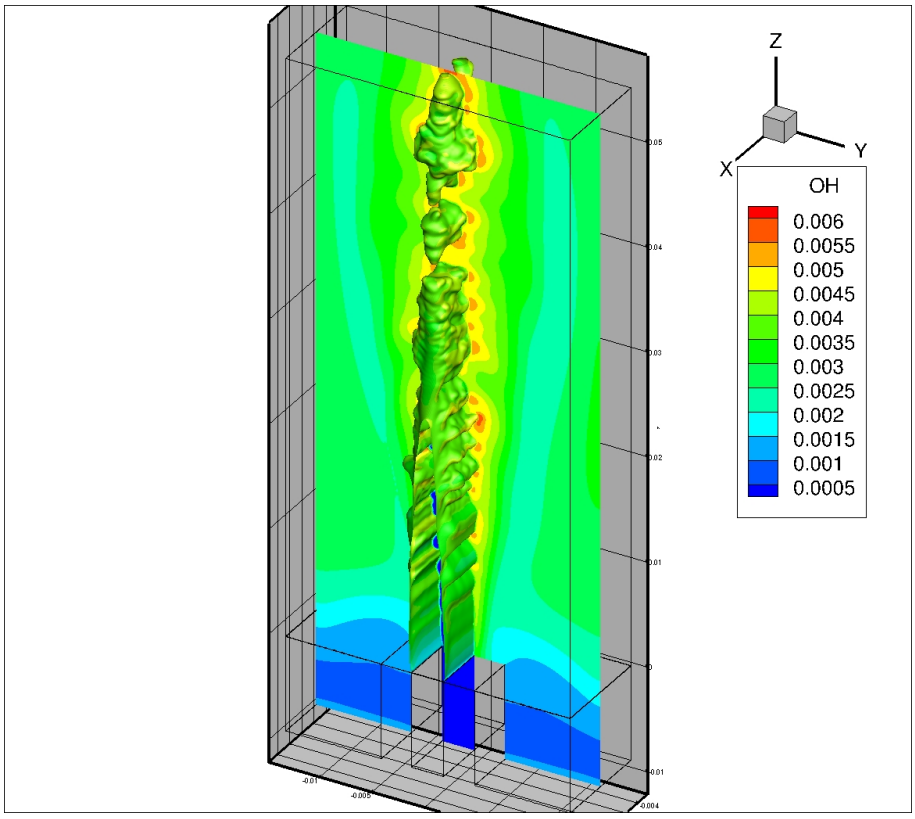

Figura 2.8: Isosurface of T at 1850K and slice of OH mass fraction.

3 Conclusions

Three-dimensional DNS of turbulent premixed slot CH4–Air flame has been carried out using detailed kinetics. A general description of the flames was provided , evidencing its macroscopic characteristics by means of flame surface areas and mean velocities and temperature profiles. Furthermore, topological features of the flame were also explored: statistics of curvatures, shape factors, Surface Density Function and displacement speeds of progress variable iso-surfaces are reported showing the contribution of thermal diffusion (Soret effect). A progress variable, c, has been defined as sum of four species mass fractions: CO_2 + CO + H_2O + H_2. Each individual species has its own mass diffusion coefficient (modeled according to the Hirschfelder and Curtiss law). This differential diffusion is considered in deriving the expression for the displacement speed. Its individual contributions, like the reaction, normal and tangential terms, were analyzed in details. The effects of differential diffusion are quantified based on the local equivalence ratio as a function of the progress variable curvature. Three dimensional flame curvature PDFs are found to be consistent with previous experimental and numerical studies of a similar slot stoichiometric CH4/air premixed flame. The behavior of S_d^* is determined essentially by the components S_r^*, S_n^*, S_{tt}^*. Numerical results of streamwise velocities are compared with the available experiments and DNS results show a good agreement with jet core thickness although, while showing correctly the the classical turbulent profile, they underestimate the peak velocity. This may be due to experimental error in the inlet velocities measurement. However, unlike the experimental measurements, the numerical results are able to give information about velocities even near combustion chamber walls, where for the experiments, the signal-to-noise ratio is not sufficient to obtain good results. So, DNS proves to be an affective and powerful instrument for studying without altering it, a turbulent flame.

Acknowledgments

The computing resources and the related technical support used for this work have been provided by CRESCO/ENEAGRID High Performance Computing infrastructure and its staff [1]. CRESCO/ENEAGRID High Performance Computing infrastructure is funded by ENEA, the Italian National Agency for New Technologies, Energy and Sustainable Economic Development and by Italian and European research programmes (see http://www.cresco.enea.it/english for information).

Bibliografia

[1] Ponti G. et al. The role of medium size facilities in the HPC ecosystem: the case of the new CRESCO4 cluster integrated in the ENEAGRID infrastructure. In *Proceedings of the 2014 International Conference on High Performance Computing and Simulation*, volume HPCS 2014, pages 1030–1033, 2014.

[2] M.S. Liou. A sequel to AUSM, part II: AUSM$^+$-up for All Speeds. *J. of Computational Physics*, 214:137–170, 2006.

[3] E. Giacomazzi, D. Cecere, N.M.S. Arcidiacono, G. Rossi, and F.R. Picchia. Les code development and validation. Technical Report WP4140b - CIRA-CF111310 V.1, CIRA - Italian Aerospace Research Center, November 2017. Project: Statement of Work for an Activity on Large Eddy Simulation for Application on LOx/CH4 Rocket Engines.

[4] E. Giacomazzi, D. Cecere, N.M.S. Arcidiacono, and F.R. Picchia. Approaching the Numerical Simulation of Trans- and Super- Critical Flows. In *8th European Combustion Meeting*, 18-21 April 2017. Dubrovnik, Croatia.

[5] E. Giacomazzi, D. Cecere, N.M.S. Arcidiacono, F.R. Picchia, G. Rossi, L. Cutrone, and A. Mastellone. Numerical Simulations of High-Pressure Mixing and Combustion'. In *AIAA Propulsion and Energy Forum*, number AIAA-2017-2707218. AIAA, 10-12 July. Atlanta, Georgia, USA.

[6] David H. Rudy and John C. Strikwerda. Boundary conditions for subsonic compressible Navier-Stokes calculations. *Computers & Fluids*, 9(3):327–338, sep 1981.

[7] Kevin W Thompson. Time-dependent boundary conditions for hyperbolic systems, II. *Journal of Computational Physics*, 89(2):439–461, aug 1990.

[8] Poinsot T.J. and Lele S.K. Boundary conditions for direct simulations of compressible viscous flows. *Journal of Computational Physics*, 101:104–129, 1992.

[9] M. Baum, T. Poinsot, and D. Thévenin. Accurate Boundary Conditions for Multicomponent Reactive Flows. *Journal of Computational Physics*, 116(2):247–261, feb 1995.

[10] Sutherland J.C. and Kennedy C.A. Improved boundary conditions for viscous, reacting, compressible flows. *Journal of Computational Physics*, 191:502–524, 2003.

[11] Nora Okong'o and Josette Bellan. Consistent Boundary Conditions for Multicomponent Real Gas Mixtures Based on Characteristic Waves. *Journal of Computational Physics*, 176(2):330–344, mar 2002.

[12] Polifke W. and Wall C. Non-reflecting boundary conditions for acoustic transfer matrix estimation with LES. In *Center for Turbulence Research Proceedings of Summer Program*, Summer 2002. Stanford.

[13] Klein M., Sadiki A., and Janicka J. A digital filter based generation of inflow data for spatially developing direct numerical or large eddy simulations. *J. of Computational Physics*, 186:652–665, 2003.

[14] Bird R.B., Stewart W.E., and Lightfoot E.N. *Transport Phenomena*. John Wiley and Sons, New York, 2nd edition, 2002.

[15] Wilke C.R. *J. Chem. Phys.*, 18:517–519, 1950.

[16] Kee R.J., Dixon-Lewis G., Warnatz J., Coltrin M.E., Miller J.A., and Moffat H.K. *The CHEMKIN Collection III, Transport*. Reaction Design, San Diego, 1998. www.reactiondesign.com.

[17] Mathur S., Tondon P.K., and Saxena S.C. *Molecular Physics*, 12:569, 1967.

[18] Veynante D. Poinsot T. *Theoretical and Numerical Combustion*. R.T. Edwards, Inc, 3th edition, 2012.

[19] E.R. R. Sankaran, J.H. Hawkes, T. Lu Chen, and C.K. Law. Structure of a spatially developing turbulent lean methane-air bunsen flame. *Proc. Combust. Inst.*, 31:1291–1298, 2007.

[20] J.H. Chen T. Echekki. Unsteady strain rate and curvature effect in turbulent premixed methane-air flames. *Combust. Flame*, 106:184, 1996.